ADVANCED MATERIALS
www.advmat.de

# Transparent Self-Healing Anti-Freezing Ionogel for Monolayered Triboelectric Nanogenerator and Electromagnetic Energy-Based Touch Panel

*Yifan Xia, Yan Zhu, Xinrong Zhi, Wenyu Guo, Biao Yang, Siyu Zhang, Mingyuan Li, Xin Wang,* and Caofeng Pan**

**The advent of Internet of Things and artificial intelligence era necessitates the advancement of self-powered electronics. However, prevalent multifunctional electronics still face great challenges in rigid electrodes, stacked layers, and external power sources to restrict the development in flexible electronics. Here, a transparent, self-healing, anti-freezing (TSA) ionogel composed of fluorine-rich ionic liquid and fluorocarbon elastomer, which is engineered for monolayered triboelectric nanogenerators (M-TENG) and electromagnetic energy-based touch panels is developed. Notably, the TSA-ionogel exhibits remarkable features including outstanding transparency (90%), anti-freezing robustness (253 K), impressive stretchability (600%), and repetitive self-healing capacity. The resultant M-TENG achieves a significant output power density (200 mW $m^{-2}$) and sustains operational stability beyond 1 year. Leveraging this remarkable performance, the M-TENG is adeptly harnessed for biomechanical energy harvesting, self-powered control interface, electroluminescent devices, and enabling wireless control over electrical appliances. Furthermore, harnessing Faraday's induction law and exploiting human body's intrinsic antenna properties, the TSA-ionogel seamlessly transforms into an autonomous multifunctional epidermal touch panel. This touch panel offers impeccable input capabilities through word inscription and participation in the Chinese game of Go. Consequently, the TSA-ionogel's innovation holds the potential to reshape the trajectory of next-generation electronics and profoundly revolutionize the paradigm of human–machine interaction.**

## 1. Introduction

With extensive development of Internet of Things (IoT) and artificial intelligence (AI), multifunctional electronics have attracted significant attention owing to their great potential in advanced smart devices, such as flexible circuits, wearable sensors, and touch panels.[1–3] In particular, multifunctional electronics play a vital role in realizing seamless integration with human body and harvesting various information from users and their surroundings.[4–7] Next-generation multifunctional electronics with transparent, self-healing, environment-stable, and simplified-structure features would meet the development of IoT and AI. However, a huge challenge still exists because conventional electronics consist of non-stretchable electrodes and rigid batteries. To satisfy the features of multifunctional electronics, tremendous efforts have been devoted to developing novel conductive electrodes with stretchability, high conductivity, and transparency. Generally, owing to the difficulty to stretch rigid solid-state electrodes, such as conductive metal, carbon materials, and silver nanowires (Ag NWs), the stretchability of solid-state electrodes is capable to be realized through utilizing various geometric structures or embedding into elastic substrate.[8–11] For instance, a metal-polymer composite conductor with low modulus and high elongation has been fabricated for health monitoring.[12] Moreover, a stretchable multifunctional fiber based on multi-walled carbon nanotubes (MWCNTs) has been reported for various motion sensing.[13] Additionally, a stretchable conductive film based on embedding Ag NWs below TPU film surface was reported for skin-mountable biopotential sensing.[14] However, those rigid solid-state electrodes exhibited low stretchability and optical transparency, high Young's modulus, and complicated fabrication processes, which severely limits their advancement. To overcome the above bottlenecks of rigid solid-state electrodes, conductive ionogel has been developed as an emerging material to facilitate transparent and stretchable multifunctional electronics, energy storage device, and actuators

Y. Xia, Y. Zhu, X. Zhi, W. Guo, B. Yang, S. Zhang, M. Li, X. Wang
School of Future Technology
Henan University
Kaifeng 475004, P. R. China
E-mail: xwang2008@vip.henu.edu.cn
C. Pan
CAS Center for Excellence in Nanoscience, Beijing Key Laboratory of Micro-nano Energy and Sensor,
Beijing Institute of Nanoenergy and Nanosystems
Chinese Academy of Sciences
Beijing 101400, P. R. China
E-mail: cfpan@binn.cas.cn

The ORCID identification number(s) for the author(s) of this article can be found under https://doi.org/10.1002/adma.202308424

DOI: 10.1002/adma.202308424

 

owing to deformable polymer networks and highly mobile ionic charge carriers.[15–20] For example, a soft conductive ionogel based on a mixture of silk fibroin and graphene oxide has been developed for strain/pressure sensors.[15] The graphene-based conductive ionogel was reported for recording electrocardiography and electroencephalography.[16] However, the conductivity and mechanical properties of ionogel-based multifunctional electronics easily deteriorate in case of water evaporation or harsh environment, which impedes their widespread applications in our daily life.

Furthermore, the continuous working of multifunctional electronics urgently requires facile sustainable power supplies. Fortunately, the invention of triboelectric nanogenerators (TENGs) based on the coupling of triboelectrification and electrostatic induction offers a vital solution to sustainable power supply for multifunctional electronics.[21–26] The TENG has been widely developed in a variety of fields including healthcare monitoring, renewable energy, and personal electronics.[27–29] Nonetheless, the development of monolayered TENG (M-TENG) remains a great challenge because the conventional TENGs with complicated stacked multilayer structure mainly consist of substrate/electrode/triboelectric material or electrode/triboelectric material. As an alternative conductive electrode, the ionogel has attracted considerable attention in TENG due to its excellent features, including high conductivity, transparency, low-temperature resistance, and stretchability.[30–32] Furthermore, the ionogel can also act as triboelectric materials to construct a flexible TENG.[33–35] However, a simplified-structure M-TENG based on high-conductive, transparent, freezing-tolerant, and self-healing ionogels is highly desired for multifunctional electronics.

Our surrounding wasted energy sources, such as vibration, heat, and stray magnetic field, are able to be converted into electrical energy by various strategies, including TENG.[36,37] Among them, ubiquitous stray magnetic fields existing within modern infrastructures (home appliances, lights, and electronic devices) are considered a promising electromagnetic energy (EME) source to offer continuous and sufficient power for portable electronics or commercial sensors.[38–42] The magneto-mechano-electric (MME) generator has been developed to convert the EME with low frequency magnetic fields (50 or 60 Hz) to electrical energy. For instance, the MME generator based on piezoelectric macro fiber composites and magnetostrictive multilayer amorphous $Fe_{85}B_5Si_{10}$ can generate milliwatt power under applied magnetic field below 300 μT.[41] However, the dielectric and mechanical loss of the MME results in low electrical output and low stability, which hinders its potentials in soft robotics and multifunctional electronics. In surprise, based on Faraday's induction law, human body as an antenna has been reported to harvest EME and directly convert it into electrical energy, which can power some sensors and electronics.[43,44] It is significantly important that our human body enables the conversion of ubiquitous EME in low-frequency magnetic fields into electrical energy for soft robotics, touch panels, and portable electronics.

The advent of AI and human–machine interface (HMI) has inspired rapid development of touch panels to achieve intuitive interaction between humans and display devices. Generally, touch panels based on piezoresistive and capacitive mechanisms have been widely applied. However, most typical touch panels still face the issue of rigid electrodes and external AC power supply. Despite the TENG-based touch panel has been reported to detect touching position without external AC power supply, the accurate recognition of continuous position changes is unable to be achieved due to inherent low-frequency electrical outputs of TENG.[31,45,46] Therefore, it is highly desirable to develop a novel self-powered touch panel that can perceive both point-by-point touching and continuous sliding.

Herein, we proposed a transparent, self-healing, and antifreezing ionogel (TSA-ionogel) to fabricate the M-TENG and EME-based touch panel. The TSA-ionogel is composed of amorphous high-dipole-moment poly(vinylidene fluoride-*co*-hexafluoropropylene) P(VDF-HFP) elastomer and 1-ethyl-3-methylimidazolium bis(trifluoromethyl sulfonyl) imide ($[EMI]^+$ $[TFSI]^-$ or EMITFSI) ionic liquid (**Figure 1a**). Moreover, the TSA-ionogel exhibits superior merits, including optical transparency (90%), strain (more than 600%), low maximum tensile stress (120 kPa), long-term stability (over 1 year), freezing tolerance (253 K) and self-healing capability. The resultant M-TENG based on TSA-ionogel, which simultaneously acts as triboelectric material and conductive electrode, demonstrates excellent output power density of 200 mW $m^{-2}$ and highly reliable electrical output at atmospheric environment for 1 year. Meanwhile, owing to highly reversible ion–dipole interactions between EMITFSI and P(VDF-HFP) polymer chains, the self-healing process of damaged M-TENG was easily completed in the atmospheric environment (293 K for 24 h) without extraneous solvents, materials, and thermal source. Furthermore, a wearable self-powered control interface based on arrayed M-TENG combined with microcontroller unit (MCU) has been successfully explored for wireless-controlled smart home applications. More interestingly, based on Faraday's induction law, the EME from stray magnetic fields can be converted to electrical energy through human body as antenna, which can directly serve as self-powered power supply to realize multifunctional TSA-ionogel-based epidermal touch panel based on surface-capacitive sensing mechanism. Simultaneously, the self-powered EME-based epidermal touch panel based on TSA-ionogel has successfully achieved excellent input functions, such as writing words and playing Chinese Go. Consequently, the developed TSA-ionogel demonstrates excellent potential in energy harvesting, smart electronics, and HMI.

## 2. Result and Discussion

### 2.1. Fabrication and Characterization of TSA-Ionogel

As schematically illustrated in Figure S1, Supporting Information, the TSA-ionogel was prepared by casting mixed solution (P(VDF-HFP)/EMITFSI/acetone solution) in various mixing ratios on substrate and evaporating the solvent at ambient temperature. The prepared TSA-ionogel exhibited wrinkle surface structure and a thickness of 350 μm, as shown in Figure S2, Supporting Information, in which the wrinkle structure can increase contact area to enhance electrical output of the M-TENG. The introduction of EMITFSI endowed excellent electrical conductivity of the TSA-ionogel. The influence of the EMITFSI concentration on electrical conductivity was evaluated, as shown in Figure 1b. With the increase of EMITFSI concentrations from 0 to 60 wt%, the TSA-ionogel formed a homogeneous conducting medium due

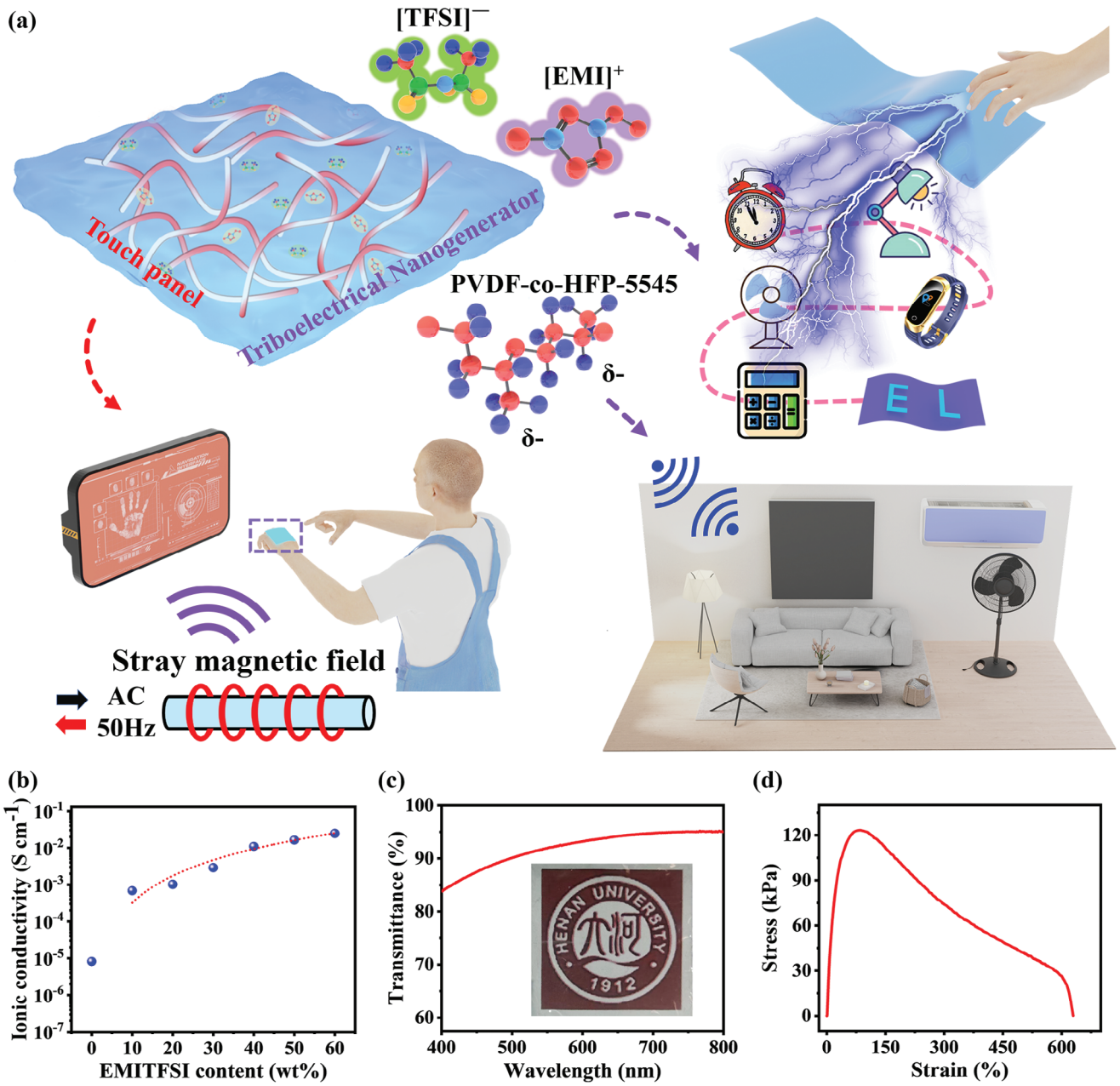


**Figure 1.** a) Schematic diagram of TSA-ionogel for portable electronics, self-powered control interface, and multifunctional epidermal touch panel. b) Electrical conductivity of TSA-ionogel with different EMITFSI concentrations. c) Transmittance spectrum of TSA-ionogel in the visible wavelength range (inset: photograph of the transparent TSA-ionogel). d) Tensile stress-strain curve of the TSA-ionogel (30 wt% EMITFSI) with a thickness of 350 µm.

to highly mobile ions ($EMI^+$ and $TFSI^-$) of ionic liquid, and its electrical conductivity increased from $10^{-5}$ to $10^{-2}$ S $cm^{-1}$. The steric hindrance from the $-CF_3$ pendant group in the —HFP provided a large free volume for the mobile ions, which contributed to high electrical conductivity. Meanwhile, high transparency and excellent stretchability are essential characteristics of next-generation multifunctional electronics, which enable visualization of internal conditions and its structures during the working process. Due to the high miscibility of EMITFSI and P(VDF-HFP), the TSA-ionogel displayed excellent transparency (over 90%) in visible light wavelengths (Figure 1c). The mechanical property of the TSA-ionogel was investigated through a tensile test, as shown in Figure 1d. The typical stress-strain curve of the TSA-ionogel showed low maximum tensile stress (120 kPa) and excellent strain capability of up to 600%.

### 2.2. Working Mechanism and Electrical Outputs of M-TENG

Conventional TENGs consist of complex stacked multilayer structures (electrode/triboelectric material), in which inherent drawbacks, including poor deformability, low mechanical

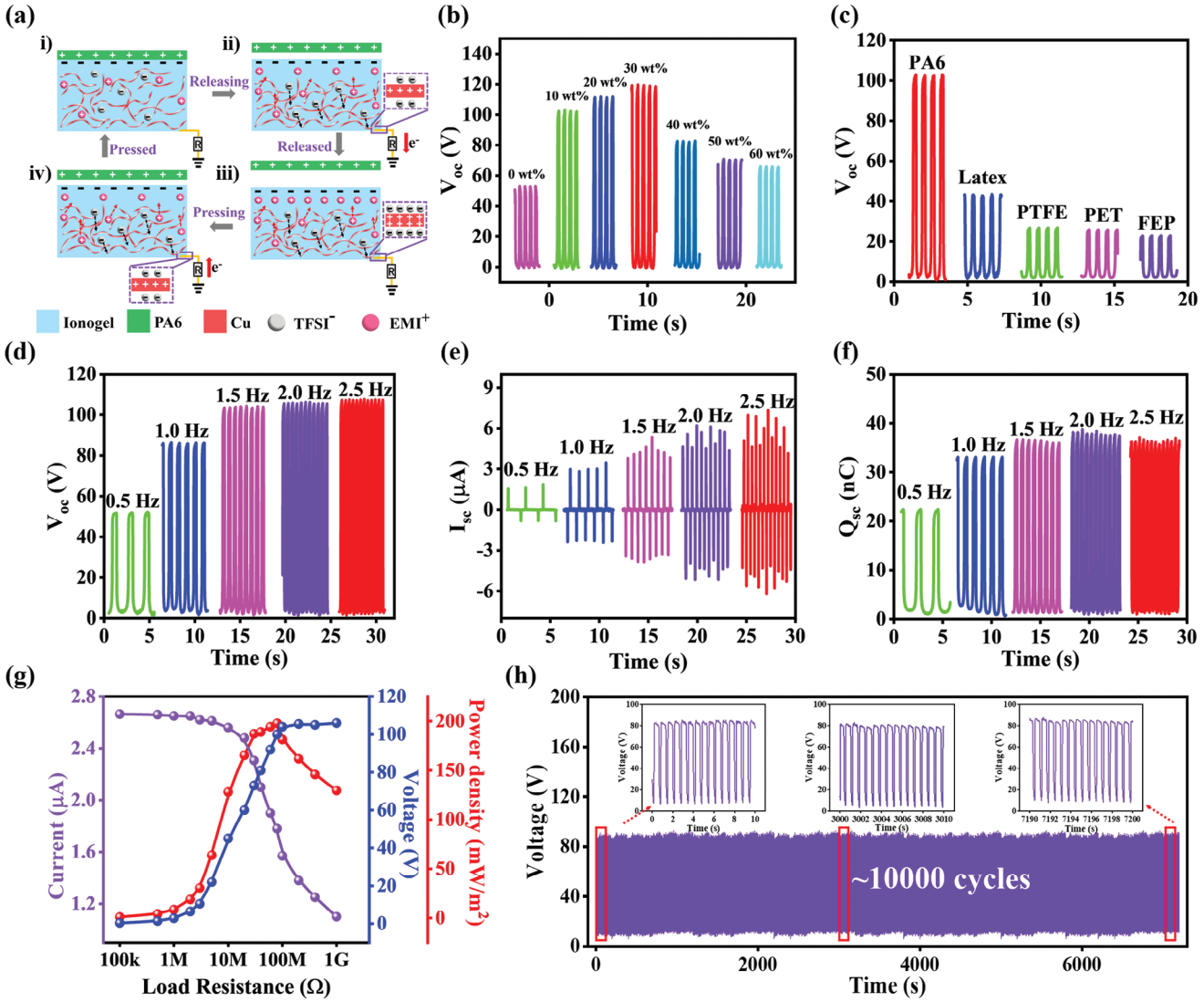


**Figure 2.** Electrical outputs of the M-TENG. a) Schematic illustration of working mechanism of the M-TENG. b) Dependence of $V_{oc}$ on the EMITFSI concentrations. c) $V_{oc}$ of the M-TENG in contact-separation with different materials. d–f) Electrical outputs ($V_{oc}$, $Q_{sc}$, and $I_{sc}$) of M-TENG under different working frequencies (0.5–2.5 Hz). g) Relationship between electrical outputs and external loads. h) Durability test of the M-TENG with 10 000 cycles under the working frequency of 1.5 Hz.

properties, and sensing resolution, lack satisfaction in portable power supplies. To address this issue, the TSA-ionogel as both triboelectric material and conductive electrode was employed for the M-TENG. The detailed working principle of the M-TENG is illustrated in **Figure** 2a, where polyamide-6 (PA6) film and TSA-ionogel serve as corresponding positive and negative triboelectric material. When PA6 film comes in contact with TSA-ionogel film completely, an equal amount of positive and negative charges is generated on the surface of PA6 film and TSA-ionogel film (Figure 2a-i), respectively. The electrostatic equilibrium exists between PA6 film and TSA-ionogel film, and the conductive cationic ($EMI^+$) and anionic ($TFSI^-$) are randomly distributed in the TSA-ionogel. When the PA6 film moves away from the TSA-ionogel, an electrical potential difference can be established between two oppositely charged surfaces. The unscreened negative charges on the surface of TSA-ionogel induce the cations ($EMI^+$) access to top negative-charged surface of TSA-ionogel and anions ($TFSI^-$) moving to the interface between TSA-ionogel and copper cable, where an electrical double layer is formed (Figure 2a-ii). Meanwhile, the electrical potential difference drives the flow of electrons from the copper to the ground via an external circuit, and an electrical signal is generated. When the separation distance between PA6 film and TSA-ionogel film reaches the maximum, the electrostatic equilibrium on the surface of TSA-ionogel can be formed and no signal is observed (Figure 2a-iii). As the PA6 film returns to contact with the TSA-ionogel film again, the electron flow in the reverse direction is generated through the external circuit (Figure 2a-iv). A continuous alternating current signal can be generated during the periodic contact-separation process.

To investigate the influences of EMITFSI concentrations on electrical outputs of M-TENG, the TSA-ionogel film with

different EMITFSI concentrations has been prepared. As shown in Figure 2b, the EMITFSI concentrations brought a considerable affection on open-circuit voltage ($V_{oc}$) of M-TENG. With an increase of the EMITFSI concentrations from 0 to 30 wt%, the $V_{oc}$ of M-TENG increased from 50 to 110 V due to an increase in the dielectric constant. The relationship between the potential difference of the M-TENG and dielectric constant can be described as:

$$V = -\frac{Q}{S_{\varepsilon_0}}\left(\frac{d_{\text{ionogel}}}{\varepsilon_r} + x(t)\right) + \frac{\sigma x(t)}{\varepsilon_0} \quad (1)$$

where $Q$ and $\sigma$ are induced charges and surface charge density on the TSA-ionogel surfaces, respectively. $\varepsilon_0$, $\varepsilon_r$, $x(t)$, $S$, and $d_{\text{ionogel}}$ are vacuum dielectric constant, dielectric constant of the TSA-ionogel, gap distance between PA6 film and TSA-ionogel film, overlapped surface area of triboelectric materials, and thickness of TSA-ionogel film, respectively. If surface charge density is a fixed value, the electrical output of M-TENG would be enhanced when increasing dielectric constant. As shown in Figure S3, Supporting Information, the dielectric constants of TSA-ionogel increased with an increase of EMITFSI concentration. However, further addition of EMITFSI concentrations in TSA-ionogel resulted in a gradual decrease of $V_{oc}$. The electrical outputs of M-TENG were affected by high-concentration EMITFSI due to the decrease in effective contact area of the triboelectric layer (PVDF-HFP) with an increase of EMITFSI content. The optimized TSA-ionogel with 30 wt% EMITFSI concentration was obtained, which was applied to further investigate the influence of different triboelectric materials and working frequencies on electrical outputs of M-TENG. A series of different triboelectric materials were used to execute in contact-separation with the TSA-ionogel film and the corresponding output voltages are shown in Figure 2c. When PA6 film acted as triboelectric material, the M-TENG exhibited superior output voltage due to greater electronegativity difference in comparison to TSA-ionogel film. Moreover, with an increase of working frequency from 0.5 to 2.5 Hz, the peak value of $V_{oc}$ exhibited a significant rise from 50 to 110 V (Figure 2d) and the short-circuit charge transfer ($Q_{sc}$) increased from 20 to 37 nC (Figure 2f). It is worth noting that the $V_{oc}$ of M-TENG increased with working frequency, which may originate from various factors, such as non-neutralized surface charges in the triboelectric layer at high frequencies and incomplete open-circuit conditions in the measuring process. Meanwhile, due to the accelerated charge transfer at high working frequency, the $I_{sc}$ was increased from 2.5 to 6.5 μA, as illustrated in Figure 2e. The dependence of the electrical outputs of M-TENG on external load resistances was further tested, as depicted in Figure 2g, in which the output voltage of M-TENG increased with an increase of resistances from $10^5$ to $10^9$ Ω, while the output current exhibited an opposite trend. The maximum value of the output power density ($P_{max}$) was calculated to be 200 mW m$^{-2}$ at an external loading resistance of 80 MΩ. Furthermore, the reliability of the M-TENG was evaluated through 10 000 contact-separation cycles at the frequency of 1.5 Hz. During this process, the output voltage presented no apparent fluctuation, as depicted in Figure 2h, which indicated an excellent durability of the M-TENG. Especially, the conductivity of TSA-ionogel stored in atmospheric environment for 1 year is consistent with the pristine one, which endows long-term electrical output stability of the M-TENG (Figure S4, Supporting Information). Therefore, the proposed TSA-ionogel based M-TENG demonstrates excellent electrical output performances.

### 2.3. Self-Healing and Anti-Freezing Performances of the M-TENG

The self-healing capability of M-TENG in atmospheric environment is highly expectant to recover its electrical outputs, which will prolong the lifetime of M-TENG. After self-healing of the damaged M-TENG in atmospheric environment, its stable electrical outputs ($V_{oc}$, $Q_{sc}$, and $I_{sc}$) are comparable with the pristine one, as shown in **Figure 3**a–c. To further evaluate the conductivity and self-healing capability, a red ink-dyed TSA-ionogel as a cable was connected with an LED and a DC power source in series, as shown in Figure S5, Supporting Information. Under the driving voltage of 3 V, the LED could be lit up, indicating excellent conductivity of the TSA-ionogel (Figure 3d). When the TSA-ionogel film was completely cut into two pieces with scissors, as shown in Figure 3e, the LED was extinguished. Two separated TSA-ionogel pieces that were in contact under atmospheric environment for 24 h were fully self-healed to construct the closed circuit, resulting in the lighting of LEDs again (Figure 3f,g). Moreover, the conductivity of self-healed TSA-ionogel (EMITFSI concentration of 60 wt%) was reduced from $0.93 \times 10^{-2}$ to $0.86 \times 10^{-2}$ S cm$^{-1}$, which exhibited a slight decay (7.5%) in comparison with the pristine one, as illustrated in Figure S6, Supporting Information.

To further investigate the self-healing capability of the TSA-ionogel with a 30 wt% EMITFSI composition, we conducted a comprehensive analysis of its tensile stress-strain behavior, as presented in Figure S7a, Supporting Information. The results revealed that the maximum tensile stress achieved by the self-healed TSA-ionogel was 105 kPa, representing a slight reduction when compared to the pristine TSA-ionogel, which exhibited a maximum tensile stress of 120 kPa. Typically, the healing efficiency is defined as the ratio of the stress or strain values exhibited by the self-healed sample ($S_h$) to those of the pristine sample ($S_p$), expressed as $H_e = S_h/S_p$. Following a self-healing duration of 24 h at room temperature (298 K), the TSA-ionogel demonstrated a remarkable healing efficiency of 91.6% for strain or 84.5% for tensile stress, as illustrated in Figure S7b, Supporting Information. The excellent self-healing capability of TSA-ionogel is due to strong interaction between the dipoles of P(VDF-HFP) polymer chains and the cations in ionic liquid. Furthermore, the anti-freezing capability of M-TENG is extremely crucial in harsh cold conditions. The conductivity of TSA-ionogel at 253 K increased from $8.19 \times 10^{-6}$ to $5 \times 10^{-3}$ S cm$^{-1}$ with an increase of EMITFSI concentrations (0–60%), as illustrated in Figure 3h, in which the conductivity was reduced with a decrease of environment temperature from 298 to 253 K due to the restricted ion mobility at low temperature. Despite the electrical outputs of M-TENG at 253 K exhibiting a slight decrease in comparison with that at 298 K due to air water vapor condensation during measurement, the energy harvesting capability in the harsh cold conditions was still satisfactory (Figure 3i–k).

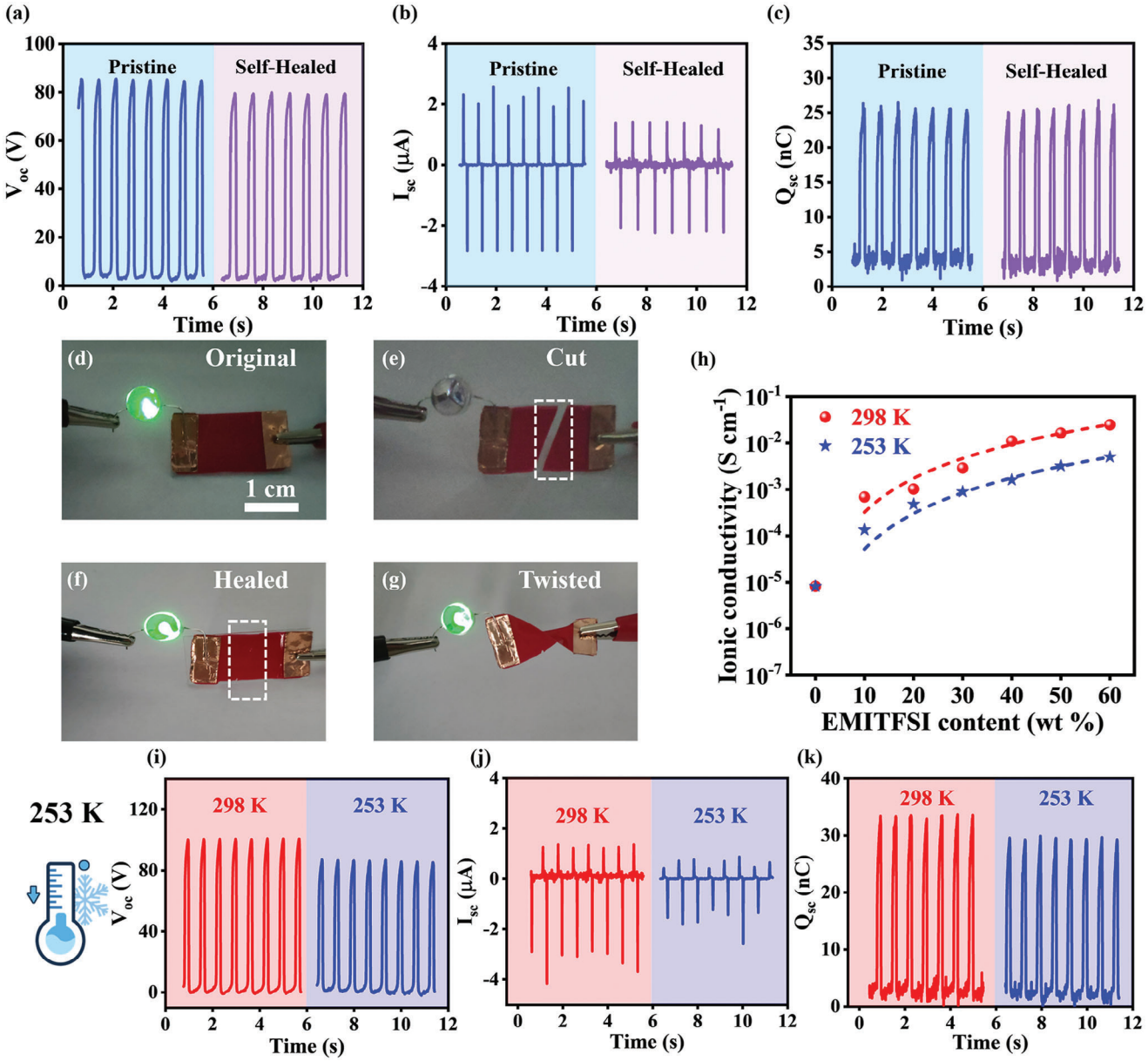


**Figure 3.** Self-healing and anti-freezing performances of the M-TENG. a–c) The electrical outputs ($V_{oc}$, $Q_{sc}$, and $I_{sc}$) of self-healed M-TENG in comparison with pristine one. d–g) Self-healing process of the TSA-ionogel. h) Ionic conductivity of the TSA-ionogel at 253 and 298 K, respectively. i–k) The electrical outputs of M-TENG at 253 and 298 K, respectively.

Furthermore, we conducted measurements of the electrical outputs of the M-TENG at temperatures exceeding room temperature, specifically within the range of 303 to 333 K. The results of these measurements are presented in Figure S8, Supporting Information. Clearly, the M-TENG exhibited consistent and stable electrical outputs that exhibited no significant dependence on temperature variations across the range from 303 to 333 K. This observation underscores the temperature-insensitive nature of the M-TENG's electrical performance within this elevated temperature range. Therefore, the M-TENG based on TSA-ionogel demonstrated excellent self-healing and freezing-tolerant performances.

### 2.4. Demonstration of M-TENG to Power Portable Electronics and EL Device

Inspired by high electrical outputs, the M-TENG was utilized as power supply to power portable electronics and EL device. The electric energy generated by M-TENG can be stored in commercial capacitors. **Figure** 4a shows the corresponding electrical management circuit that consists of bridge rectifier and commercial capacitors, which convert alternating current into direct current for charging capacitors. As shown in Figure 4b, various capacitors (0.22, 0.47, 1.0, and 2.2 μF) can be successfully charged by the M-TENG under working frequency of 1.5 Hz,

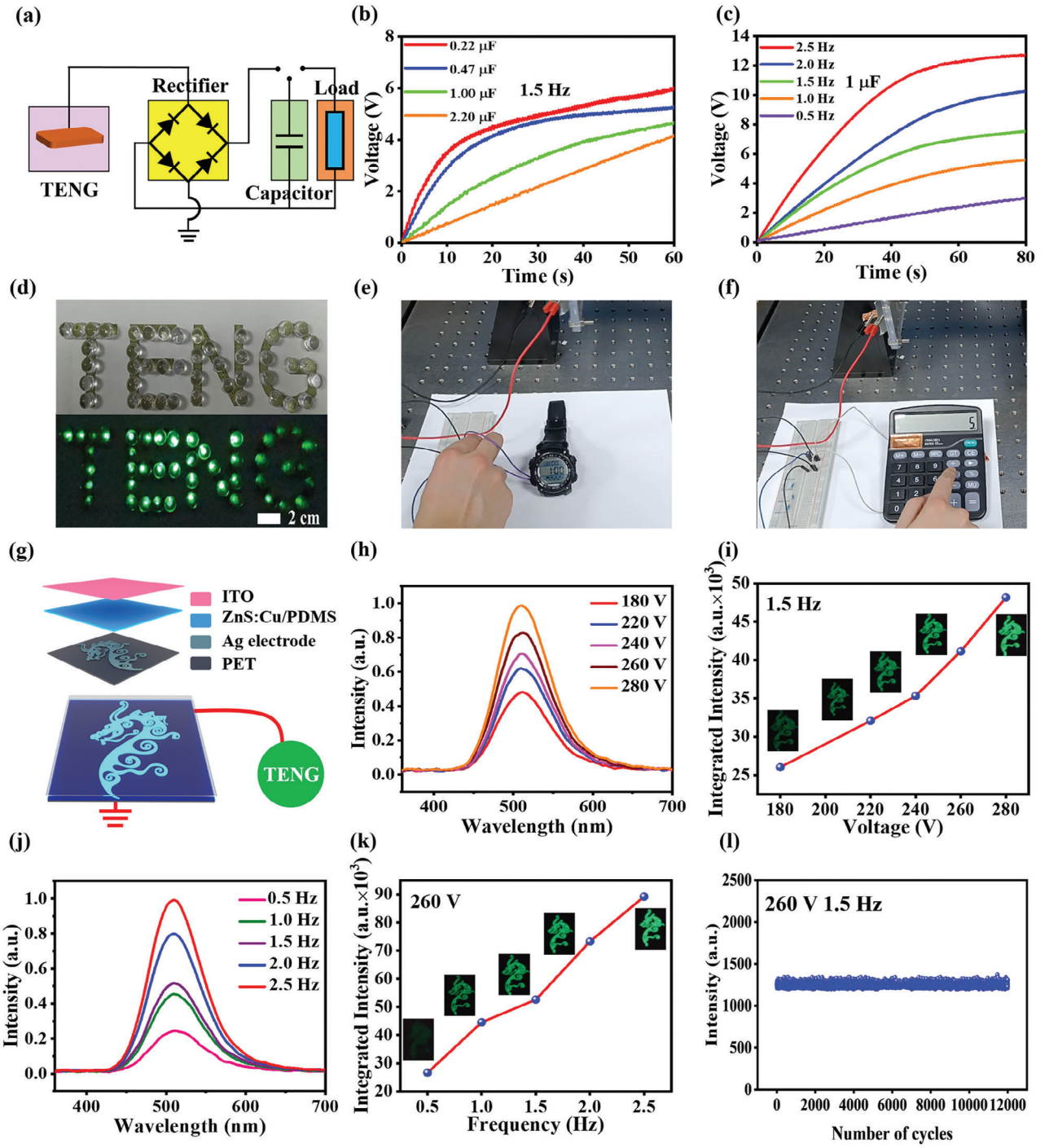


**Figure 4.** Demonstration of the M-TENG as a power supply to power the portable electronics and EL device. a) Equivalent electrical circuit diagram for charging system to power portable electronics. b,c) Relation of charging voltage with various capacitors and different motion frequencies. d–f) Photographs of powering LED, electronic watch, and calculator. g) Detailed structure of self-powered EL. h,i) EL spectra and intensity of the EL device under different driving voltage (180–280 V) of M-TENG. j,k) EL spectra and intensity of the EL device under driving of M-TENG at different working frequencies (0–2.5 Hz). l) Durability testing of EL device (12 000 cycles).

in which a capacitor of 2.2 μF can be charged to 4.0 V within only 60 s. Meanwhile, the charging speed (1.0 μF) increased markedly with increasing working frequencies from 0.5 to 2.5 Hz (Figure 4c). To demonstrate great potential of the M-TENG as power supply, a commercial capacitor charged by M-TENG can successfully drive electronic watch, calculator, and more than 45 green LEDs, respectively, as shown in Figure 4d–f (Movies S1–S3, Supporting Information). Furthermore, a self-powered EL display device was developed by assembling the M-TENG and EL device based on patterned silver electrode, which further indicated

the potential of M-TENG as power supply. The detailed structure of self-powered EL display device is schematically illustrated in Figure 4g, where an emission layer of ZnS: Cu-embedded PDMS was sandwiched between a transparent indium tin oxide (ITO) electrode and a dragon-patterned silver electrode connecting with the M-TENG through copper wires. The alternating current EL (ACEL) is widely recognized as a basic structure of high-field EL, in which the injected electrons from the electrode can be accelerated to become "hot" electrons to collide with luminescent centers under an applied high AC voltage. Subsequently, the luminescent center in excited state occurs radiative transition to the ground state, followed by the light emission. Benefiting from the excellent AC output performance, the M-TENG can directly power the dragon-patterned EL device without external power supply (Movie S4, Supporting Information). To investigate optical performance of the fabricated EL display device, the corresponding EL spectra and intensity were evaluated under different driving voltages of 180–280 V (Figure 4h,i). The corresponding electrical outputs of the M-TENG (60 × 60 $mm^2$) are shown in Figure S9, Supporting Information. With an increase of the driving voltage from 180 to 280 V, the EL intensity was enhanced by 1.99-fold at the working frequency of 1.5 Hz due to the amplification in energy and the quantity of hot electrons. The correlation between driving voltage and luminescent brightness can be elucidated through Lehmann Model, followed by the formula:

$$L = A\exp\left[\left(-\frac{B}{V^{\frac{1}{2}}}\right)\right] \quad (2)$$

where $V$ is the driving voltage, $L$ is the luminance, both $A$ and $B$ are constants. Moreover, under a driving voltage of 260 V of M-TENG, the EL intensity also increased significantly with the working frequency increased from 0.5 to 2.5 Hz, as shown in Figure 4j,k, consistent with our previously reported results.[20,47] Subsequently, the repeatability and stability of self-powered EL display device were further investigated under a long-term powering of the M-TENG. As illustrated in Figure 4l, the EL intensity can be sustained even after 12 000 cycles, indicating excellent repeatability and durability of the M-TENG.

### 2.5. Self-Powered Control Interface for Wireless-Controlled Smart Home Appliances

Furthermore, a self-powered control interface based on an arrayed M-TENG was developed for wireless-controlled smart home appliances, which was composed of analog-to-digital converter (AD620), MCU (Arduino Uno), electromagnetic relay, and Bluetooth module (HC-05). The conceptual diagram of self-powered control interface is shown in **Figure** 5a. When human finger touches the self-powered control interface attached to the forearm, the voltage signals will be generated for a wireless-controlled smart home appliance. Figure 5b exhibits the flow chart and the corresponding equivalent circuit modules of the self-powered control interface. The voltage signals generated from the arrayed M-TENG can be converted into digital signal by analog-to-digital converter (Figure 5c,d). The generated digital signals are sent through signal transmitter to wireless signal receiver to establish wireless communication through the wireless module that consists of MCU and Bluetooth modules, as shown in Figure 5b. The MCU in wireless signal receiver sends the corresponding command signal to electromagnetic relay for accurate switching on or off of smart home appliances (Movie S5, Supporting Information), such as fan, bulb, alarm, and hydrometer as a proof of concept. The photograph of corresponding self-powered control interface based on the arrayed M-TENG is displayed in Figure 5e. Moreover, these signals generated by the M-TENG can be easily separated from noisy crosstalk signals due to adequate voltage output. Therefore, the developed self-powered control interface based on the arrayed M-TENG has expanded the applications of TENG in smart home appliances.

### 2.6. Demonstration of Self-Powered Epidermal Touch Panel

Based on Faraday's induction law, human body as a special antenna is able to convert EME from ubiquitous stray magnetic field into electrical energy,[43,48,49] which will provide a novel insight and strategy to develop advanced self-powered touch panel. To the best of our knowledge, it has not been reported that the electrical energy converted by the EME is utilized as power supply for self-powered epidermal touch panel. As shown in **Figure** 6a-i, when human body encounters stray magnetic fields, the periodic voltage signals can be induced on human body due to magnetic flux change. The induced voltage signal was detected through an oscilloscope, as shown in Figure S10a, Supporting Information, in which the positive electrode of oscilloscope was connected with human fingertip and the negative electrode was grounded. The EME-induced voltage signal of human fingertip was ≈1.5 V with a frequency about 50 Hz that is consistent with the EM signals generated by surrounding infrastructures. To ascertain the source of the induced voltage signals, we also conducted measurements of voltage oscillograms arising from triboelectric and capacitive effects, respectively. When compared with the EME-induced voltage signal (1.5 V, 50 Hz), the voltage output generated by the M-TENG exhibited a higher amplitude (4.0 V) and a lower frequency (0.6 Hz), in line with the inherent properties of TENGs (as depicted in Figure S10b, Supporting Information).

Furthermore, in order to assess the potential influence of capacitive effects on the voltage signal, we quantified the resistance ($R_i$) from the human fingertip to the end of the TSA-ionogel and the capacitance ($C_{finger}$) at the fingertip/TSA-ionogel interface, obtaining approximate values of 30 MΩ and 6 nF, respectively (as presented in Figure S10c, Supporting Information). A simulation of the voltage signal within the resulting RC circuit was performed using Multisim, revealing that the voltage ($V_c$) observed at both ends of the $C_{finger}$ amounted to only 20 mV, which was negligible due to the low capacitance of 6 nF (as demonstrated in Figure S10d, Supporting Information). Therefore, our investigations provide strong evidence that the detected voltage signal from the touch panel predominantly originates from the magnetic field and is not significantly influenced by other effects, such as triboelectric or capacitive interactions. Additionally, these EME-induced voltage signals were applicable across the human body regardless of individual difference or body parts. To verify its applicability, the EME-induced voltage signals on different body parts (including hand, elbow, and forehead) were recorded

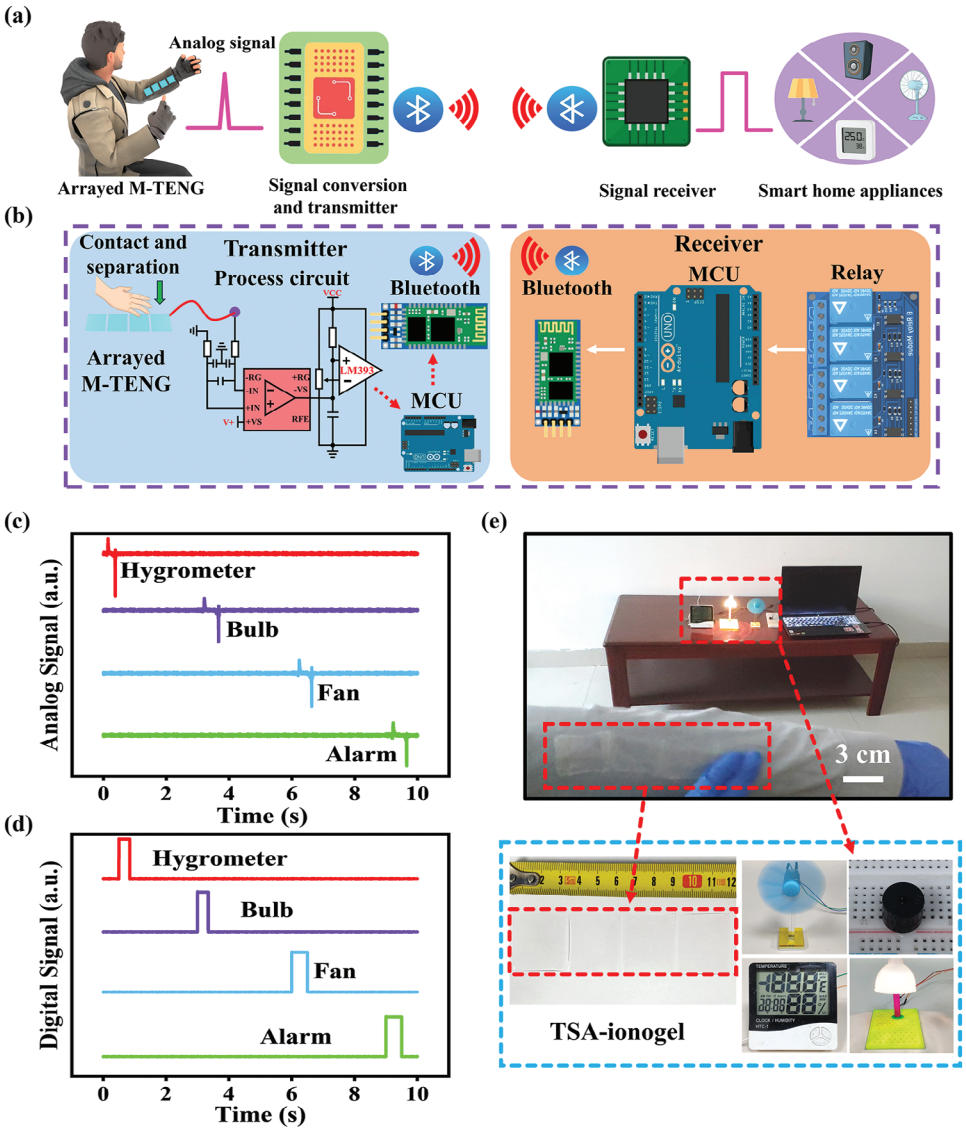


**Figure 5.** Self-powered control interface based on the M-TENG. a) Schematic diagram of the self-powered control interface for wireless-controlled smart home appliances. b) Equivalent electrical circuit diagram of self-powered control interface, consisting of M-TENG and wireless control module (microcontroller unit (MCU), electromagnetic relay, and Bluetooth module). c) Analog signal generated by finger typing the M-TENG. d) Digital signal generated by circuit processing. e) Photograph of self-powered control interface.

for five volunteers, as shown in Figure S11, Supporting Information. The recorded voltage signals exhibited an identical electrical characteristic, which was independent on the parts of human body. Moreover, a similar EME-induced voltage signal could also be detected at the external resistance ($R_e$ = 10 MΩ) that was connected in series with human body, as shown in Figure 6a-iii. Although the EME-induced voltage output from stray magnetic field is much smaller than that of other energy harvesters, the stable voltage output has a great potential in a novel self-powered touch panel.

Inspired by the EME-induced voltage signal, the self-powered multifunctional epidermal touch panel has been developed to achieve an easy and intuitive HMI. As shown in Figure 6a-ii, a 1D touch panel (10 × 60 mm$^2$) based on the TSA-ionogel strip was employed to display the position-sensing capability. Both ends of the TSA-ionogel strip were connected in series with a $R_e$ within a closed circuit. The corresponding simplified equivalent circuit of touch panel is shown in Figure 6a-iv. The electrical double-layer capacitance ($C_{EDL}$) was formed at the electrode/TSA-ionogel interface and a coupling capacitance ($C_{finger}$) was formed at the fingertip/TSA-ionogel interface, allowing alternating current to flow from the fingertip to the ground. The 1D touch panel could be considered as a resistance ($R_i$) that is divided into two parts by the fingertip. The resistance value of each part is proportional to its normalized length, that is, $x$ and $1 - x$. Figure 6b further demonstrates the position-sensing capability of TSA-ionogel-based touch panel. When the point-by-point touching of human fingertip from left to right is performed on the 1D touch panel, $xR_i$ increases and the $V_1$ voltage signal decreases, while $(1 - x)R_i$ decreases and the $V_2$ voltage signal increases.

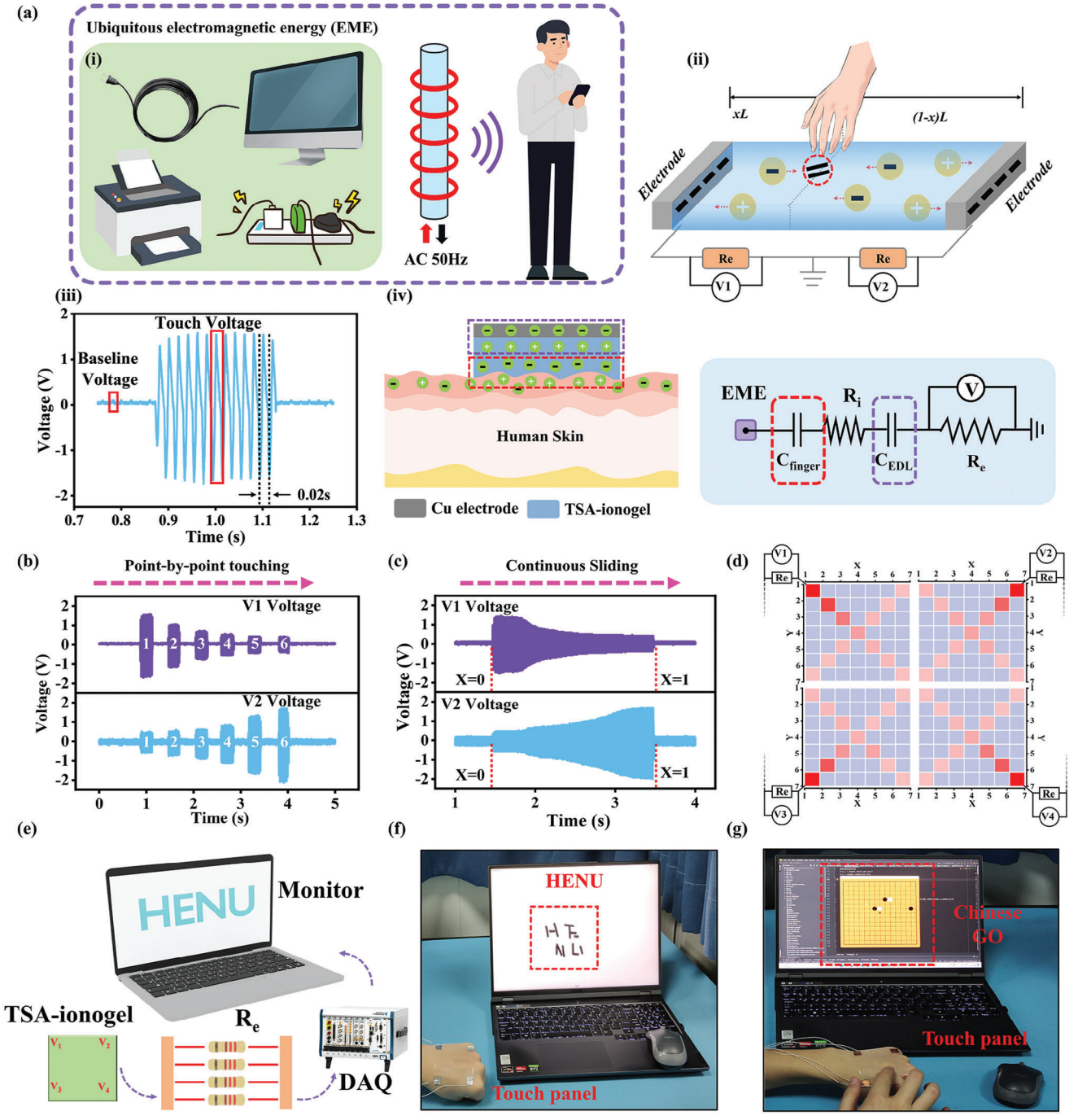


**Figure 6.** Self-powered epidermal touch panel. a) Working mechanism of the touch panel based on Faraday's induction law. b,c) The corresponding $V_1$ and $V_2$ voltage signals when a point-by-point touching or continuous sliding of human fingertip from left to right on the touch panel. d) Mapping of peak voltage detected by DAQ during a human fingertip touching corresponding positions on the touch panel. e) Schematic diagram of self-powered epidermal touch panel, composed of TSA-ionogel film, $R_e$, DAQ, and monitor. f,g) Demonstrations of the multifunctional touch panel when writing the words "HENU" (abbreviation of Henan University) and playing Chinese Go, respectively.

The EME-induced voltage signals measured on each side of 1D touch panel are inversely proportional to the distance between the touch position and the corner. Meanwhile, when the fingertip continuously slides on the touch panel, as shown in Figure 6c, the corresponding changes in EME-induced voltage signals and the resistances also exhibit a similar trend. To accurately identify the touch position, a TSA-ionogel-based 2D touch panel (60 × 60 $mm^2$) was developed based on the same position-sensing mechanism as the 1D touch panel. The voltage signals ($V_1$, $V_2$, $V_3$, and $V_4$) at each corner of the touch panel were recorded with a point-by-point touching along the diagonal lines of the touch panel, as shown in Figure 6d. Upon contact of the human

fingertip with the 2D touch panel, the system can be conceptually divided into four parallel resistances contingent upon the touch position. Each of these resistances within the circuit is connected in series with a $R_e$ (Figure S12b, Supporting Information). An additional clarification of the operational principles of the EME-based touch panel is provided. Simulations of the electric potential distribution across the surface of the touch panel were achieved by using COMSOL Finite Element Analysis (FEA). The simulation results, as illustrated in Figure S12c, Supporting Information, depict the outcome when a human fingertip engages in a point-by-point touching motion from left to right across the touch panel's surface. These results reveal that the area in close proximity to the fingertip exhibits a higher electric potential, while the areas further away from the fingertip display lower electric potential values. The findings derived from the COMSOL FEA simulations are consistent with the voltage mapping presented in Figure 6d, thereby providing robust empirical evidence that substantiates the reliability and trustworthiness of the EME-induced voltage signal. Therefore, the touching position coordinate on the 2D touch panel can be calculated by using the peak voltages, which have an inverse relationship with the coordinates, followed by the equations:

$$x \propto \frac{V_2 + V_4}{V_1 + V_2 + V_3 + V_4} \tag{3}$$

$$y \propto \frac{V_1 + V_2}{V_1 + V_2 + V_3 + V_4} \tag{4}$$

where $x$ and $y$ are coordinate of the touch position, $V_1$, $V_2$, $V_3$, and $V_4$ are the peak voltages of each corner of the 2D touch panel. Based on Equations (3) and (4), the touch position coordinates can be calculated and transmitted to the computer to achieve accurate position recognition. Moreover, the operations of self-powered touch panel in different extreme environments and bending states were examined, as shown in Figure S13, Supporting Information, almost similar voltage signals were recorded, indicating consistent position-sensing capability at subzero temperature (253 K) and different bending states. Furthermore, it is noteworthy that the EME-induced voltage exhibits a strong correlation with the distance separating the human body from surrounding infrastructures. As this distance progressively extends from 0.05 to 4.0 meters, a corresponding decrease in the EME-induced voltage is observed, diminishing from 3.5 to 0.6 V. This observed dependency aligns with the anticipated spatial distribution characteristics of the magnetic field, as delineated in Figure S14, Supporting Information.

To ascertain the origin of the induced voltage signal, we conducted measurements using an Electric Magnetic Field (EMF) detector to assess both the electric field intensity and the magnetic field intensity in the proximity of a fingertip. As depicted in Figure S15, Supporting Information, the electric field intensity in the vicinity of the fingertip was determined to be negligible, effectively registering at zero. Conversely, the magnetic field intensity was quantified at 0.06 μT, thus establishing that the presence of this magnetic field induces a voltage signal at the fingertip when our human body functions as an antenna. It is unequivocal that the EME-induced voltage is predominantly attributed to the magnetic field and not to the electric field. To further demonstrate excellent input functions of the 2D touch panel, a multifunctional epidermal touch panel has been fabricated by connecting a monitor, TSA-ionogel film, and multi-channel data acquisition system (DAQ), as shown in Figure 6e. When the fingertip touched the 2D touch panel, the EME-induced voltage signals from each $R_e$ were recorded and transmitted to a personal computer through an independent channel of DAQ. After receiving these EME-induced voltage signals, the coordinates of touching position were calculated by computer to achieve various applications. For instance, based on this touch panel, some applications, including writing letters (HENU, abbreviations of Henan University) and playing Chinese Go, have been successfully demonstrated on the monitor (Figure 6f,g, Movies S6 and S7, Supporting Information). It is worth noting that during the experiments, the level of EM radiation in our lab was less than 0.5 μT, as shown in Figure S16, Supporting Information, which meets safety standard (less than 100 μT) of International Commission on Non-Ionizing Radiation Protection. Therefore, the developed self-powered multifunctional epidermal touch panel demonstrates excellent flexibility, freezing tolerance, and input functions, which would offer potential applications in wearable electronics, IoT, and HMI.

## 3. Conclusion

In summary, the TSA-ionogel has been developed as a propitious candidate for the realization of high-performance M-TENG and EME-based touch panel. The TSA-ionogel exhibited noteworthy attributes of remarkable transparency (90%), pronounced freeze tolerance (253 K), excellent stretchability (600%), and the self-healing ability, attributed to the robust miscibility and profound interaction between P(VDF-HFP) and EMITFSI. The performance evaluation of M-TENG (30 × 30 $mm^2$), constructed by utilizing the TSA-ionogel with an EMITFSI concentration of 30%, elucidated its exceptional peak power density reaching 200 mW $m^{-2}$, along with its sustained and reliable electrical output profile over 1 year. Furthermore, the M-TENG's proficiency in biomechanical energy harvesting was exhibited through powering an EL display device and diverse portable electronic devices (such as electronic watches, calculators, and LEDs) without external power supplementation. Concurrently, a self-powered control interface has been devised to facilitate the wireless regulation of smart home appliances. Most significantly, the TSA-ionogel-based self-powered multifunctional epidermal touch panel, underpinned by Faraday's induction law, has been conceived and validated. This configuration convincingly demonstrated remarkable input functionalities upon the epidermal touch panel, such as writing the word "HENU" and engaging in the game of Chinese Go. Consequently, the proposition of the TSA-ionogel not only extends a spectrum of captivating prospects within the domains of next-generation wearable electronics but also finds its applicability within the realms of soft robotics, HMI, and among others.

## 4. Experimental Section

Detailed experimental materials and methods can be found in the Supporting Information.

*Ethical Statement*: Ethical approval (HUSOM2023-273) was obtained from the Henan University research ethics committee, and informed written consent of all volunteers was obtained.

## Supporting Information

Supporting Information is available from the Wiley Online Library or from the author.

## Acknowledgements

Y.X. and Y.Z. contributed equally to this work. The authors gratefully acknowledge financial support from the National Natural Science Foundation of China (no. 11774384, 52125205, 52250398, U20A20166, 52192614, and 52003101) and the Natural Science Foundation of Henan (no. 232300421215).

## Conflict of Interest

The authors declare no conflict of interest.

## Data Availability Statement

The data that support the findings of this study are available from the corresponding author upon reasonable request.

## Keywords

electromagnetic energy, ionogel, multifunctional electronics, self-powered touch panel, triboelectric nanogenerator

Received: August 19, 2023
Revised: November 7, 2023
Published online: December 1, 2023

[1] K. Dong, X. Peng, Z. L. Wang, *Adv. Mater.* **2020**, *32*, 1902549.
[2] G. Gao, F. Yang, F. Zhou, J. He, W. Lu, P. Xiao, H. Yan, C. Pan, T. Chen, Z. L. Wang, *Adv. Mater.* **2020**, *32*, 2004290.
[3] D. Kim, *Nat. Electron.* **2023**, *6*, 405.
[4] Y. Lee, J. Park, A. Choe, S. Cho, J. Kim, H. Ko, *Adv. Funct. Mater.* **2019**, *30*, 1904523.
[5] H. Liu, W. Wei, L. Zhang, J. Xiao, J. Pan, Q. Wu, S. Ma, H. Dong, L. Yu, W. Yang, D. Wei, H. Ouyang, Y. Liu, *Adv. Funct. Mater.* **2021**, *31*, 2104088.
[6] N. Rodeheaver, R. Herbert, Y.-S. Kim, M. Mahmood, H. Kim, J.-W. Jeong, W.-H. Yeo, *Adv. Funct. Mater.* **2021**, *31*, 2104070.
[7] S. Wang, Y. Nie, H. Zhu, Y. Xu, S. Cao, J. Zhang, Y. Li, J. Wang, X. Ning, D. Kong, *Sci. Adv.* **2022**, *8*, eabl5511.
[8] J.-H. Kim, S.-R. Kim, H.-J. Kil, Y.-C. Kim, J.-W. Park, *Nano Lett.* **2018**, *18*, 4531.
[9] M. Kim, H. Lim, S. H. Ko, *Adv. Sci.* **2023**, *10*, 2205795.
[10] H. Wang, Z. Rao, Y. Liu, L. Shan, T. Guo, H. Chen, R. Wang, *Nano Energy* **2023**, *107*, 108170.
[11] J.-H. Tian, R.-H. Fan, P.-T. Yang, H.-K. Wu, S. Jiang, Y.-L. Zhou, A. K. Sarychev, *Rare Met.* **2023**, *42*, 3318.
[12] J. Cheng, J. Shang, S. Yang, J. Dou, X. Shi, X. Jiang, *Adv. Funct. Mater.* **2022**, *32*, 2200444.
[13] K. Y. Chung, B. Xu, Z. Li, Y. Liu, J. Han, *Chem. Eng. J.* **2023**, *454*, 140384.
[14] W. Zhou, S. Yao, H. Wang, Q. Du, Y. Ma, Y. Zhu, *ACS Nano* **2020**, *14*, 5798.
[15] F. He, X. You, H. Gong, Y. Yang, T. Bai, W. Wang, W. Guo, X. Liu, M. Ye, *ACS Appl. Mater. Interfaces* **2020**, *12*, 6442.
[16] J. Park, S. Lee, M. Lee, H.-S. Kim, J. Y. Lee, *Small* **2023**, *19*, 2300250.
[17] M. Wu, X. Wang, Y. Xia, Y. Zhu, S. Zhu, C. Jia, W. Guo, Q. Li, Z. Yan, *Nano Energy* **2022**, *95*, 106967.
[18] X. Yao, S. Zhang, L. Qian, N. Wei, V. Nica, S. Coseri, F. Han, *Adv. Funct. Mater.* **2022**, *32*, 2204565.
[19] Y. Zhao, Y. Ohm, J. Liao, Y. Luo, H.-Y. Cheng, P. Won, P. Roberts, M. R. Carneiro, M. F. Islam, J. H. Ahn, L. M. Walker, C. Majidi, *Nat. Electron.* **2023**, *6*, 206.
[20] Y. Zhu, Y. Xia, M. Wu, W. Guo, C. Jia, X. Wang, *Nano Energy* **2022**, *98*, 107309.
[21] F.-R. Fan, Z.-Q. Tian, Z. Lin Wang, *Nano Energy* **2012**, *1*, 328.
[22] J. Wang, C. Wu, Y. Dai, Z. Zhao, A. Wang, T. Zhang, Z. L. Wang, *Nat. Commun.* **2017**, *8*, 88.
[23] Z. L. Wang, *ACS Nano* **2013**, *7*, 9533.
[24] S. Hajra, A. M. Padhan, B. K. Panigrahi, P. Pakawanit, Z. Jagličić, N. Vittayakorn, Y. K. Mishra, S. Lee, H. J. Kim, *J. Materiomics* **2023**, https://doi.org/10.1016/j.jmat.2023.09.011.
[25] X. Hou, J. Zhong, C. Yang, Y. Yang, J. He, J. Mu, W. Geng, X. Chou, *J. Materiomics* **2022**, *8*, 958.
[26] H. Zhang, D.-Z. Zhang, D.-Y. Wang, Z.-Y. Xu, Y. Yang, B. Zhang, *Rare Met.* **2022**, *41*, 3117.
[27] L. Wang, W. Liu, Z. Yan, F. Wang, X. Wang, *Adv. Funct. Mater.* **2020**, *31*, 2007221.
[28] Z. Yan, L. Wang, Y. Xia, R. Qiu, W. Liu, M. Wu, Y. Zhu, S. Zhu, C. Jia, M. Zhu, R. Cao, Z. Li, X. Wang, *Adv. Funct. Mater.* **2021**, *31*, 2100709.
[29] S. Zhu, Y. Xia, Y. Zhu, M. Wu, C. Jia, X. Wang, *Nano Energy* **2022**, *96*, 107116.
[30] Y. Cao, Y. J. Tan, S. Li, W. W. Lee, H. Guo, Y. Cai, C. Wang, B. C.-K. Tee, *Nat. Electron.* **2019**, *2*, 75.
[31] Y. Lee, S. Lim, W. J. Song, S. Lee, S. J. Yoon, J.-M. Park, M.-G. Lee, Y.-L. Park, J.-Y. Sun, *Adv. Mater.* **2022**, *34*, 2108586.
[32] Y. Ren, Z. Liu, G. Jin, M. Yang, Y. Shao, W. Li, Y. Wu, L. Liu, F. Yan, *Adv. Mater.* **2021**, *33*, 2008486.
[33] Y. Kim, D. Lee, J. Seong, B. Bak, U. H. Choi, J. Kim, *Nano Energy* **2021**, *84*, 105925.
[34] P. Nellepalli, M. P. Kim, J. Park, S. M. Noh, Z. Ye, H. W. Jung, H. Ko, J. K. Oh, *ACS Appl. Mater. Interfaces* **2022**, *14*, 17806.
[35] D. L. Vu, C. P. Vo, C. D. Le, K. K. Ahn, *Int. J. Energy Res.* **2021**, *45*, 8960.
[36] J.-D. Musah, A. M. Ilyas, S. Venkatesh, S. Mensah, S. Kwofie, V. A. L. Roy, C.-M. L. Wu, *Nano Res. Energy* **2022**, *1*, 9120034.
[37] K. Wang, W. Xu, W. Zhang, X. Wang, X. Yang, J. Li, H. Zhang, J. Li, Z. Wang, *Nano Res. Energy* **2023**, *2*, 9120042.
[38] V. Annapureddy, M. Kim, H. Palneedi, H.-Y. Lee, S.-Y. Choi, W.-H. Yoon, D.-S. Park, J.-J. Choi, B.-D. Hahn, C.-W. Ahn, J.-W. Kim, D.-Y. Jeong, J. Ryu, *Adv. Energy Mater.* **2016**, *6*, 1601244.
[39] V. Annapureddy, S.-M. Na, G.-T. Hwang, M. G. Kang, R. Sriramdas, H. Palneedi, W.-H. Yoon, B.-D. Hahn, J.-W. Kim, C.-W. Ahn, D.-S. Park, J.-J. Choi, D.-Y. Jeong, A. B. Flatau, M. Peddigari, S. Priya, K.-H. Kim, J. Ryu, *Energy Environ. Sci.* **2018**, *11*, 818.
[40] M. G. Kang, R. Sriramdas, H. Lee, J. Chun, D. Maurya, G. T. Hwang, J. Ryu, S. Priya, *Adv. Energy Mater.* **2018**, *8*, 1703313.
[41] H. Lee, R. Sriramdas, P. Kumar, M. Sanghadasa, M. G. Kang, S. Priya, *Energy Environ. Sci.* **2020**, *13*, 1462.
[42] J. Ryu, J.-E. Kang, Y. Zhou, S.-Y. Choi, W.-H. Yoon, D.-S. Park, J.-J. Choi, B.-D. Hahn, C.-W. Ahn, J.-W. Kim, Y.-D. Kim, S. Priya, S. Y. Lee, S. Jeong, D.-Y. Jeong, *Energy Environ. Sci.* **2015**, *8*, 2402.

[43] M. V. Boskovic, M. Frantlovic, E. Milinkovic, P. D. Poljak, D. V. Radovic, J. N. Stevanovic, M. Sarajlic, *Chemosensors* **2023**, *11*, 51.
[44] J. Li, Y. Dong, J. H. Park, J. Yoo, *Nat. Electron.* **2021**, *4*, 530.
[45] Z. Hu, X. Hui, S. Li, L. Tang, J. Sun, H. Zeng, J. Chen, H. Guo, *Nano Energy* **2023**, *114*, 108676.
[46] H. Park, S.-J. Oh, D. Kim, M. Kim, C. Lee, H. Joo, I. Woo, J. W. Bae, J.-H. Lee, *Adv. Sci.* **2022**, *9*, 2201070.
[47] Y. Xia, Y. Zhu, B. Yang, W. Guo, S. Han, X. Wang, *Nano Energy* **2022**, *102*, 107653.
[48] Z. Ren, J. Nie, L. Xu, T. Jiang, B. Chen, X. Chen, Z. L. Wang, *Adv. Funct. Mater.* **2018**, *28*, 1805277.
[49] Y. Zhang, K. Zhang, Y. Shi, Z. Li, D. Zhao, Y. Pi, Y. Cui, X. Zhou, Y. Zhang, J. Zhong, *Mater. Today Energy* **2022**, *29*, 101131.